

CHAPTER 3: IMAGE PROCESSING AND DEPTH ESTIMATION METHODS

Magnetic field data are used for a variety of reasons, the most basic of which is to probe the subsurface. Very often, the image derived from the data does not show sufficiently detailed structure. This chapter deals with (1) image processing of data with particular reference to upward continuation and automatic gain control and (2) depth estimation using Euler deconvolution and wavenumber estimation methods. Upward-continuation will be used to emphasize long-wavelength anomalies as this helps to compare ground magnetic data with aeromagnetic data. The automatic gain control method helps to enhance subtle features. Euler deconvolution and wavenumber depth estimation help to identify the position and depth of selected features within the area. A discussion of the methods and applications to synthetic data is given below. The methods will be used to analyse the data in Chapter 4.

3.1 Upward continuation

Upward continuation is a transformation whereby the potential field anomaly is calculated at an altitude higher than the measured field. Because of this and because the size of dipole magnetic anomalies decreases with the cube of the distance from the source, the original data are smoothed. Jacobsen (1987) likened upward continuation to a low pass filter because high frequency components are attenuated while low frequency components are enhanced. The mathematical description of upward continuation is summarised below. A detailed description can be found in Gibert and Galdeano (1985).

$A(x,y,z)$ is assumed to be a potential field at location x,y,z and to be harmonic outside the source. In the absence of a source in the upper half space, A is given by Gibert and Galdeano (1985) as

$$\Delta[A(x, y, z)] = 0 \text{ where } z \geq 0. \quad 3.1$$

If values of A are known on the surface $z = 0$, the function can be continued upward in the upper half space. By utilizing Green's integration, $A(x,y,z)$ ($z > 0$) can be determined from $A(x,y,0)$. This is expressed as follows (Schwartz, 1950)

$$A(x, y, z) = \frac{z}{2\pi} \int_{-\infty}^{\infty} \int_{-\infty}^{\infty} \frac{A(\xi, \eta, 0)}{[(x - \xi)^2 + (y - \eta)^2 + z^2]^{3/2}} d\xi d\eta \quad 3.2$$

Equation 3.2 can be expressed as a product of a convolution, which can be written as

$$A(x, y, z) = A(x, y, 0) * P_z(x, y) \quad 3.3$$

where

$$P_z(x, y) = \frac{z}{2\pi(x^2 + y^2 + z^2)^{3/2}} \quad 3.4$$

Rewriting Equation 3.3 as a convolution product of the respective Fourier Transforms yields

$$\tilde{A}_z(u, v) = \tilde{A}_0(u, v) \tilde{P}_z(u, v) \quad 3.5$$

Consider a function $g(x,y)$ whose Fourier Transform is defined as follows

$$\tilde{g}(u,v) = \int_{-\infty}^{\infty} \int_{-\infty}^{\infty} g(x, y) \exp[-2i\pi(ux + vy)] dx \cdot dy \quad 3.6$$

while the inverse Fourier Transform of $g(x,y)$ is given by

$$g(x, y) = \int_{-\infty}^{\infty} \int_{-\infty}^{\infty} \tilde{g}(u, v) \exp[2i\pi(ux + vy)] du \cdot dv \quad 3.7$$

where $i^2 = -1$ (Bracewell, 1965).

The above relation allows for simplification of Equation 3.7 and this gives the Fourier transform

$$\tilde{P}_z(u, v) = \exp(-2\pi\rho z) \quad 3.8$$

$$\text{where } \rho^2 = u^2 + v^2 \quad 3.9$$

Substituting Equation 3.9 into Equation 3.5 yields

$$\tilde{A}_z(u, v) = \tilde{A}_0(u, v) \exp(-\kappa z), \quad \kappa = 2\pi\rho \quad 3.10$$

where κ is the wavenumber and z is the continuation height.

Equation 3.2 is also known as the upward continuation equation in the space domain while Equation 3.10 is the equivalent in the frequency domain.

FORTTRAN codes that calculate upward-continuation of potential fields have been published by Gibert and Galdeano (1985). Descriptions of the programs and input data format are also given in the paper.

3.1.1 Application of upward-continuation on synthetic data

The effectiveness of the upward-continuation filter was tested on synthetic data (Fig. 3.1) before applying to real data (Chapter 4). The synthetic model consisted of two rectangular blocks (marked 1 and 2, Fig. 3.1) and a vertical dyke (marked 3). The

dimensions, positions, depths and magnetization of the bodies are given in Table 3.1. The parameters of the ambient field are: inclination = -63.8° and declination = -18.6° .

Table 3.1. Geometrical and magnetic parameters of the synthetic sources generating the total-field magnetic anomaly of Fig. 3.1.

Source	Magnetization (A/m)	X range (m)	Y range (m)	Depth range (m)
1	1	300-800	400-1000	20-1000
2	3	500-600	550-650	20-50
3	3	200-800	105-112	10-300

Fig. 3.1 shows the response of anomalies with different wavelengths to upward continuation to a height of 150 m. The smaller rectangular block (2) and narrow dyke (3) do not show visible anomalies in the upward continued map (Fig. 3.1c). This is consistent with the upward continuation algorithm as it tends to suppress subtle features at the expense of longer wavelength anomalies. Fig. 3.1b is the theoretical magnetic response of the model calculated at a height of 150 m. Ideally Figs. 3.1b and 3.1c should be similar. However, the shape of the anomaly is not quite the same at the top of the figures, probably due to the window size used in the upward continuation (Fig. 3.1c). In general the shape of the anomaly in Fig. 3.1c can be controlled by altering the window size. Despite the differences in anomaly size in Figs. 3.1b and 3.1c the above exercise illustrates that upward continuation can be used successfully to compare ground magnetic data with aeromagnetic data.

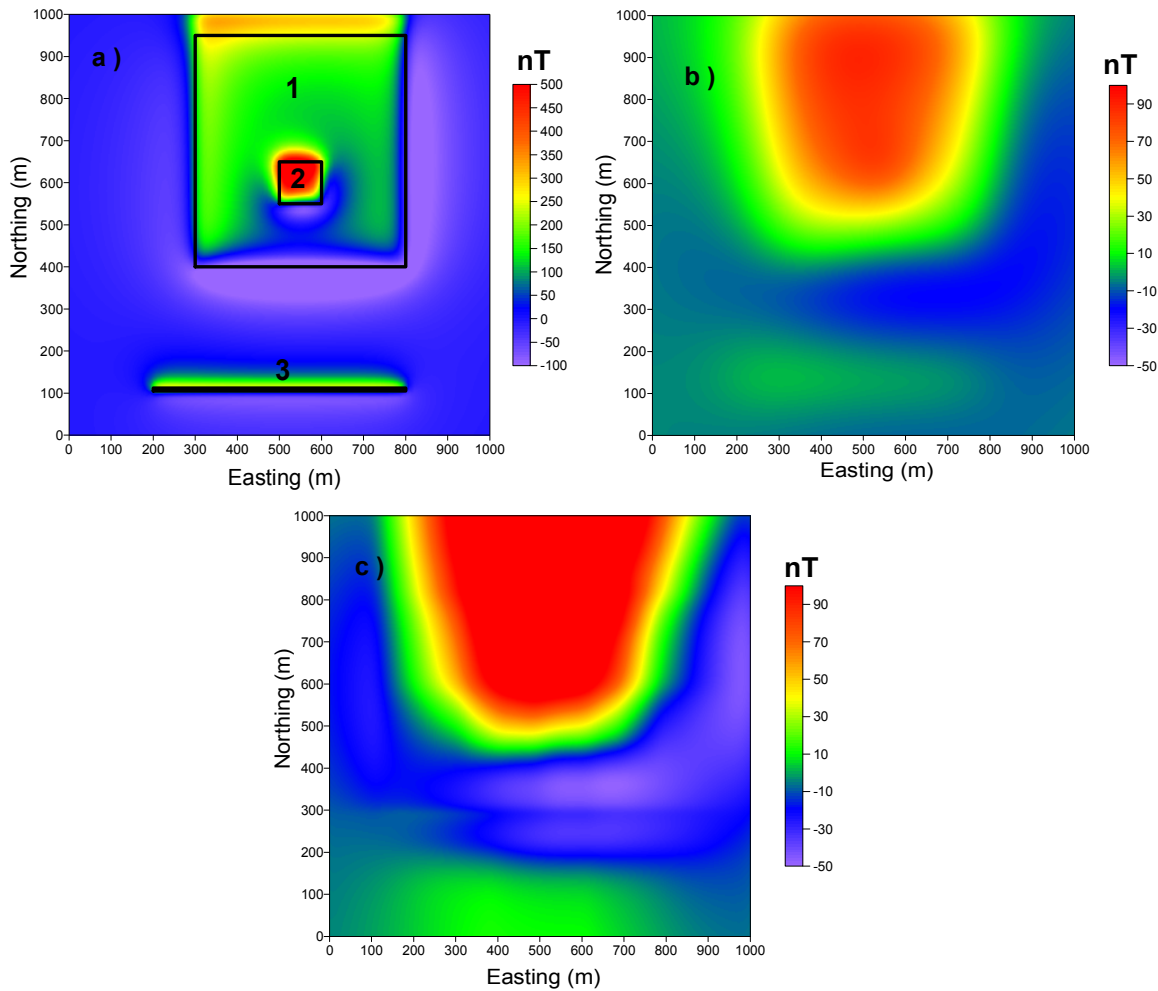


Figure 3.1. Synthetic magnetic data for testing upward-continuation. a) Raw data (observation height at 2.5 m), b) magnetic attraction of bodies in (a) calculated at a height of 150 m, c) data from (a) upward continued to 150 m. Note that (1-3) are the outlines of the sources of the respective anomalies. For example 1 belongs to the larger rectangle.

3.2 Automatic gain control (AGC) of map data

Perhaps the most important use of magnetic images is to indicate areas of considerable magnetic contrast and to visualize features such as faults and dykes, which are depicted as lineaments. Because the amplitude of anomalies depends on magnetic field strength and depth of source rocks, lower amplitude anomalies are often suppressed at the expense of high amplitude anomalies. Rajagopalan and Milligan (1995) noted that subtle features

can be highlighted by increasing their relative amplitudes and by emphasising the continuity of the features.

There are many techniques that have been employed to achieve image enhancement. Some of the best readily used filters are the horizontal derivative, the vertical derivative, and sunshading. Horizontal and vertical gradient filters are used to highlight subtle features, as well as accentuate discontinuities and breaks in anomaly trends. In particular, vertical gradient maps emphasise short-wavelength features and attenuate long-wavelength anomalies. Sunshading is a directional filter that is used to enhance features in certain directions and suppress those features which are perpendicular to the desired direction (Cooper, 2001). It is a combination of the two horizontal gradients. However, it is evident that using the sunshading filter, wholesale image enhancement is not possible as one has to choose the direction of interest. The image enhancement required here is one where both short-wavelength and long-wavelength anomalies must be preserved. Therefore, using all of the above mentioned filters is not an optimal exercise.

To overcome the above dilemma, Rajagopalan (1987) and Rajagopalan and Milligan (1995) used automatic gain control (AGC) to enhance the amplitude of short-wavelength anomalies without diminishing long-wavelength anomalies.

The AGC for grid data is given by

$$A_{xy} = (Gain_{xy})(F_{xy}) \quad 4.1$$

where,

$$F_{xy} = Input \text{ (Input = Data to be analysed)}$$

$$Gain_{xy} = \frac{1}{(2v+1)(2w+1)} \left[\sum_{i=x-v}^{i=y+v} \sum_{i=x-w}^{i=x+w} F_{ij}^p \right]^r \quad 4.2$$

$A_{xy} = Output$ (Output = Data after AGC operation)

power = p

root = r

$$\text{and the window size} = \frac{1}{(2v+1)(2w+1)} \quad 4.3$$

F_{xy} is the input function with dimensions x and y, and v and w are the dimensions of the window. Appendix A.2 is the MATLAB implementation of Equation 4.2.

The input waveform, which constitutes multiple amplitudes, is adjusted such that the output waveform is of constant amplitude using the following steps. 1) The amplitude of the input signal is calculated using the root mean square (RMS) value. 2) The gain function of the amplifier (which is taken as inversely proportional to the RMS value obtained from the above) is calculated. 3) The last step involves calculating the output function, which depends on the window size.

The gain function can be made to be equal to the inverse of the RMS value provided p and r are substituted by 2 and 0.5 in Equation 4.2 respectively. Rajagopalan, (1987) and Rajagopalan and Milligan (1995) observed that if the input signal is made up of variable amplitudes but constant wavelength, by setting the window length to the same value as the wavelength, the output signal will have constant amplitude.

3.2.1 Pitfalls in using automatic gain control for the processing of magnetic data

Any geophysical tool used to interrogate magnetic data has its benefit and limitations that any user must be cognizant of before one uses it. One such advantage of the AGC method is the enhancement of trends and subtle features in magnetic data.

However, this method is very sensitive to the length of the window. To illustrate the point, a window size that is too small will amplify values to ± 1 and that a window size that is too large will result in an output signal that is similar to the input signal (Rajagopalan, 1987). This clearly shows that the choice of the window size is critical for attaining a good output signal. A number of window sizes should be tested in order to produce an output that best enhances the lower amplitude signals (Rajagopalan, 1987; Rajagopalan and Milligan, 1995).

Rajagopalan and Milligan (1995) showed that the AGC method works best when applied on profile data compared with gridded data. They created two AGC images, the first produced from profiles (AGC was applied to each profile separately then stacked together to create a map) and the second from gridded data. In the first approach the AGC was applied to the total magnetic intensity (TMI) profiles and the grid was created from these AGC profiles. The second approach differed from the first approach in that the AGC was directly applied to the TMI grid.

They observed that the trends and subtle features were adequately enhanced in the map created from AGC profiles than those seen in the map created from gridded data. They also found that when the AGC is applied to gridded data, 3-dimensional anomalies were well represented compared with those from the other approach. In both cases they also observed that the AGC was amplifying noise in the data, particularly when the AGC was applied to gridded data. The problem with noise is not so severe so that the effectiveness of the method should be in doubt.

The disadvantages with creating AGC images using the first approach (gridding is performed on the AGC profiles) include more processing time, and also require a lot of computer memory (Rajagopalan and Milligan, 1995).

In the scenario where the user has to apply the AGC method to a large data set is it better to use the second approach (directly apply the AGC to gridded data) as this will greatly reduce the processing time.

The above were taken into account in the applications of the AGC method that will follow below.

3.2.2 Application of automatic gain control to synthetic data

The automatic gain control algorithm was applied to synthetic data before applying it to real data (Chapter 4). The aim of this exercise was to ascertain the reliability of the method, i.e. its effectiveness in identifying hidden features (which can be of different dimensions). The synthetic model consisted of five dykes (marked 1-5, Fig. 3.2) and a rectangular block (marked 6). The dimensions, positions, depths and magnetization of the bodies are given in Table 3.2. The parameters of the ambient field are similar to that used in Section 3.1.1. Fig. 3.2 shows the magnetic response of the models given in Table 3.2. Note that anomalies of some bodies have smaller amplitude so that it is difficult to see them in Fig. 3.2a.

Table 3.2. Geometrical and magnetic parameters of the synthetic sources generating the total-field magnetic anomaly of Fig. 3.2. Note that the units of the inclination angles of the sources are in degrees.

Source	Magnetization (A/m)	Inclination of source	X range (m)	Y range (m)	Depth range (m)
1	3	-63.8	365-372	400-800	10-300
2	0.5	63.8	400-407	400-800	10-300
3	0.1	63.8	800-807	400-800	10-300
4	0.1	-63.8	200-800	212-219	10-300
5	0.5	-63.8	200-800	30-37	10-300
6	0.05	-63.8	550-580	550-580	10-300

Figs. 3.3 and 3.4 show the applications of AGC along profiles taken from Fig. 3.2. The aim of this exercise as stated above is to enhance weak signals in the original data. In Fig. 3.3a anomalies that correspond to source bodies 2, 3 and 6 are barely visible. However, after the application of the AGC filter with window sizes 51 (102 m in ground units, Fig. 3.3c) and window size 201 (402 m in ground units, Fig. 3.3d) these anomalies are enhanced considerably. The distinction between anomaly 1 and 2 is very difficult, this is perhaps due to the fact that these two anomalies are separated by a mere 28 meters, which is less than the window sizes used for this exercise. A window size of 11 (32 m in ground units, Fig. 3.3b) does not yield a favourable results as the shape of the anomalies appear to be distorted, which suggests that optimal results are obtained for relatively bigger window sizes, i.e. 102 and 402 meters.

In Fig. 3.4 the same results are seen for window size 102 m and 402 yielding reasonable results and for window size 32 m with anomalies that appear to be distorted with respect to the original data (Fig. 3.4a).

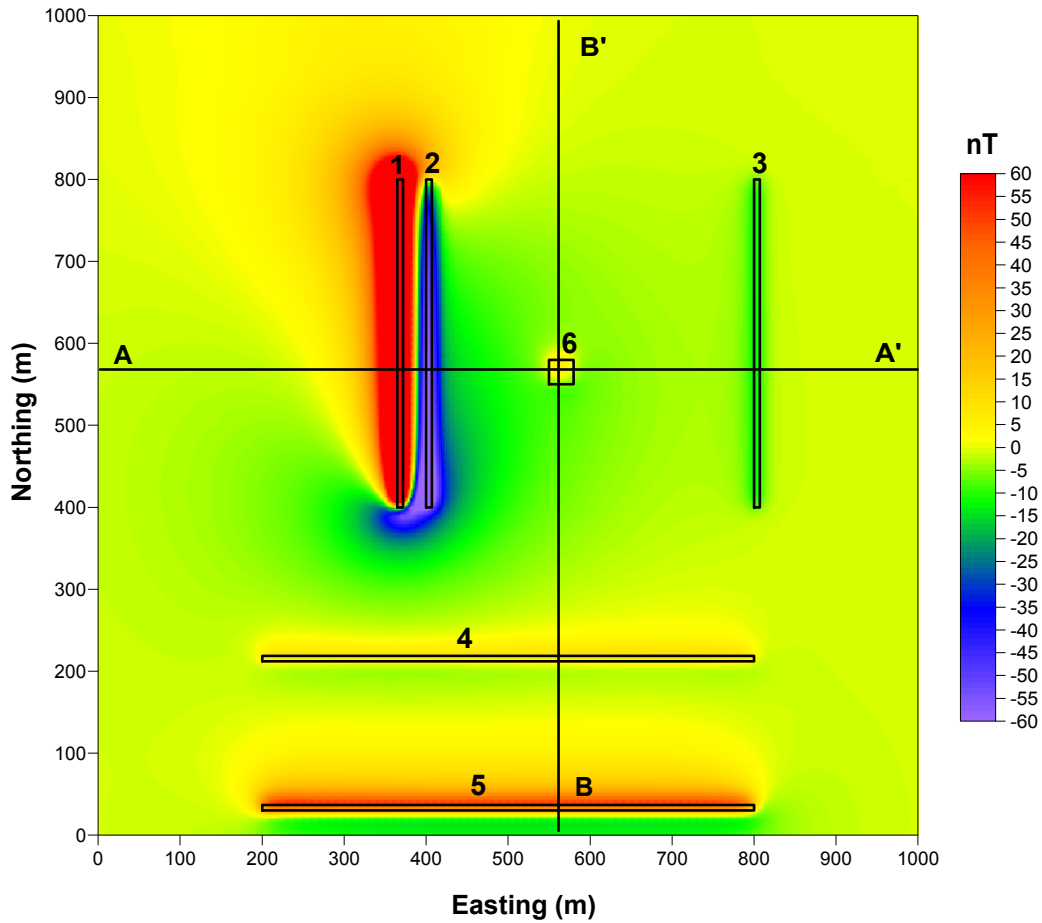


Figure 3.2. The total magnetic anomaly due to the synthetic model given in Table 3.2. The numbers 1-6 are the source bodies, and the lines A-A' and B-B' are the position of the profiles used in the AGC analysis (Figs. 3.3 and 3.4). Note that the image was “clipped” from -60 nT to 60 nT in order to have a good overall contrast.

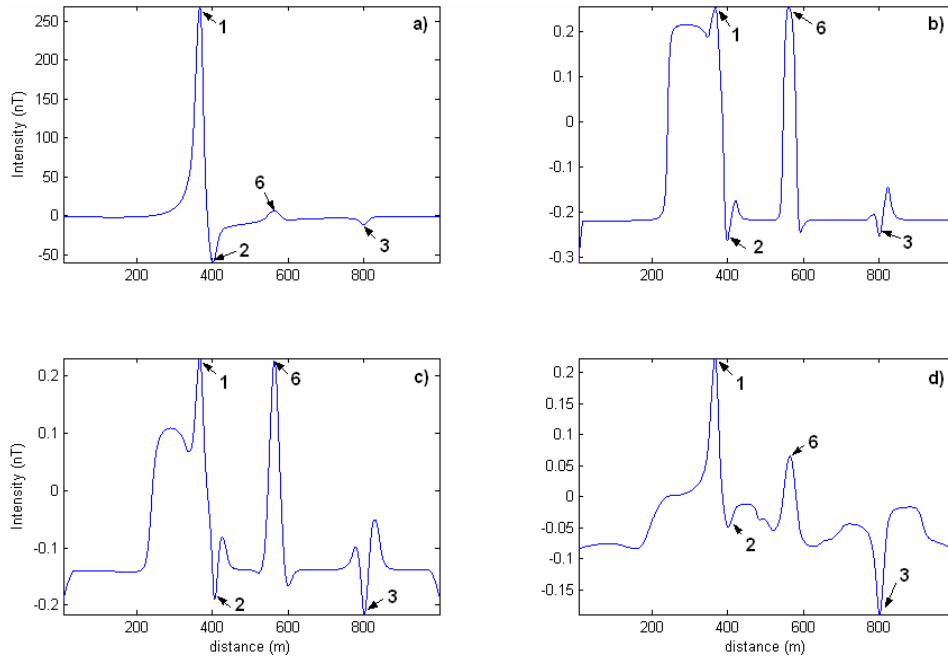


Figure 3.3. AGC applied to profile A-A' (Fig. 3.2) (a) for window sizes, b) 32 m, c) 102 m and d) 402 respectively. The numbers (1, 2, 3 and 6) are the positions of the anomalies associated with the bodies in Table 3.2.

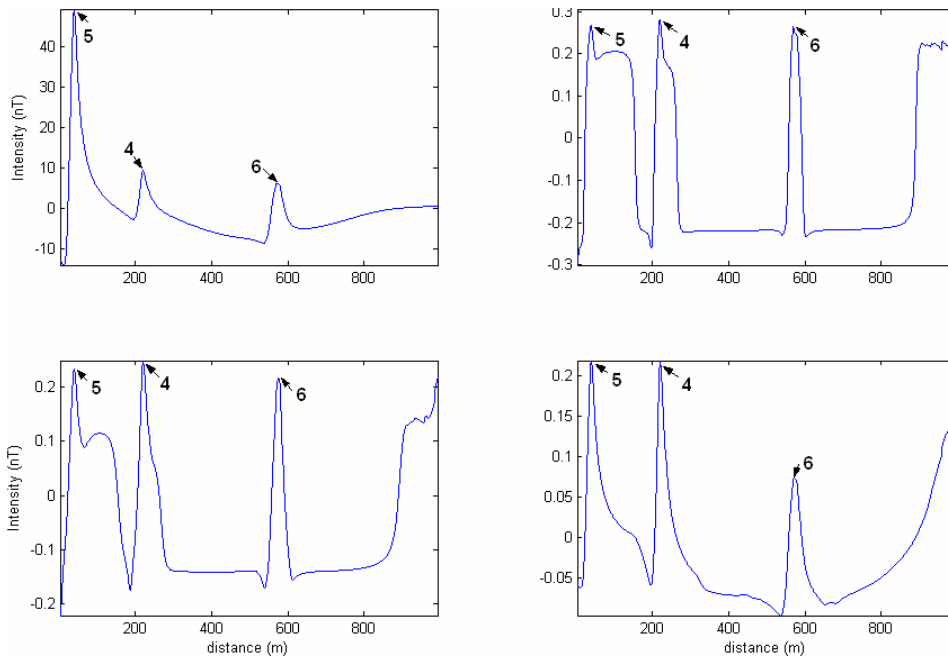


Figure 3.4. AGC applied to profile B-B' (Fig. 3.2). Figures a–d as in Fig. 3.3. The numbers (4 -6) are the positions of the anomalies associated with the bodies in Table 3.2.

3.3 Quantitative interpretation of depth sources of potential fields

In this section, two methods for automatic depth interpretation are discussed. The methods are applied to synthetic data to assess their reliability and depth estimates are compared. The computer programs used for Euler deconvolution were provided by A. Galdeano (personal communication, 2005). All programs that involve calculating depth using the wavenumber method were coded by the author in MATLAB (Appendix A.2) incorporating some code from G. Cooper (personal communication, 2005). These programs will be used to calculate depths of a prominent feature along selected profiles in Chapter 4.

3.3.1 Local wavenumber

Bracewell (1965) defined f (the local frequency) as the rate of change of the local phase (M) with respect to x . Thus f can be expressed mathematically as

$$f = \frac{1}{2\pi} \frac{\partial}{\partial x} \tan^{-1} \left[\frac{\partial M}{\partial z} / \frac{\partial M}{\partial x} \right] \quad 3.20$$

Defining the local wavenumber in terms of frequency

$$\kappa = 2\pi f . \quad 3.21$$

substituting Equation 3.20 into Equation 3.21 we get

$$\kappa = \frac{1}{|A|^2} \left(\frac{\partial^2 M}{\partial x \partial z} \frac{\partial M}{\partial x} - \frac{\partial^2 M}{\partial x^2} \frac{\partial M}{\partial z} \right). \quad 3.22$$

Equation 3.22 is the expression of the local wavenumber for profile data (Thurston and Smith, 1997). Note that M must be differentiable at least up to order two. Appendix A.3 provides the MATLAB algorithm to calculate Equation 3.22.

For gridded data it has been shown by Huang and Versnel (2000) that the wavenumber is given by

$$\begin{aligned} \kappa = & \frac{1}{M_x^2 + M_y^2 + M_z^2} \\ & \times \left\{ M_x \left[M_{zz} - \frac{M_z}{M_x^2 + M_y^2} (M_x \cdot M_{xx} + M_y \cdot M_{xy}) \right] \right. \\ & \left. + M_y \left[M_{zy} - \frac{M_z}{M_x^2 + M_y^2} (M_x \cdot M_{xy} + M_y \cdot M_{yy}) \right] \right\} \end{aligned} \quad 3.23$$

By considering a sloping contact, the expressions for the vertical and horizontal gradients as defined by Nabighian (1972) are given by

$$\frac{\partial M}{\partial z} = 2KFc \sin d \frac{x \cos(2I - d - 90) - h \sin(2I - d - 90)}{h^2 + x^2} \quad 3.24$$

$$\frac{\partial M}{\partial x} = 2KFc \sin d \frac{h \cos(2I - d - 90) + x \sin(2I - d - 90)}{h^2 + x^2} \quad 3.25$$

where K is the susceptibility contrast, F is the magnitude of the ambient field, $c = 1 - \cos^2 I \sin^2 \alpha$, α is the ambient field declination, I is the inclination of the ambient field, d is the angle of dip of the body and h is the depth to the top of the contact.

Substituting Equation 3.24 and Equation 3.25 into Equation 3.23 gives

$$\kappa = \frac{h}{h^2 + x^2} \quad 3.26$$

If it is assumed that the peaks coincide with the edges of the bodies, and letting $x = 0$, then the local depth can be written as

$$h = \frac{1}{\kappa} \quad (\text{Thurston and Smith, 1997}). \quad 3.27$$

Equation 3.27 is the expression used to calculate the local depth over maxima from the local wavenumber for profile data. However, for gridded data the maxima are located by using the procedure given by Blakely and Simpson (1986) and later modified by Roest et al. (1992). An additional feature of the method is that it gives a linearity index, which gives the shape of the source body. As an example, Blakely and Simpson (1986) concluded that an index of 1 is indicative of a linear feature (e.g. dyke or fault) and that an index of 4 corresponds to a circular feature.

3.3.2 Euler deconvolution

The earliest published attempts to use Euler deconvolution as an alternative tool in locating depth of sources are given by Thompson (1982) for profile data and Reid et al. (1990) for gridded data. Subsequent papers have been published to address a variety of issues, including constraining solutions of the source coordinate (e.g. Fairhead et al., 1994; Barbosa et al., 1999), estimation of the structural index (Barbosa et al., 1999), and the use of extended Euler deconvolution to invert for more parameters, such as dip and susceptibility of the source body (e.g. Mushayandebvu et al., 2001)

In his treatment of the problem, Thompson (1982), considered a function in a regular Cartesian coordinate system, $f(x,y,z)$ such that z is downward, and x and y correspond to the east and north directions respectively. Assuming that $f(x,y,z)$ is homogeneous to degree n , it has to obey the following relation

$$f(tx, ty, tz) = t^n f(x, y, z) \quad 3.28$$

From the above expression the following equation (known as Euler's equation) holds equally well

$$x \frac{\partial f}{\partial x} + y \frac{\partial f}{\partial y} + z \frac{\partial f}{\partial z} = nf \quad (\text{Blakely, 1996}) \quad 3.29$$

For potential field data, and assuming a magnetic source, Euler's equation can be written as

$$(x - x_0) \frac{\partial T}{\partial x} + (y - y_0) \frac{\partial T}{\partial y} + (z - z_0) \frac{\partial T}{\partial z} = N(B - T) \quad 3.30$$

where (x_0, y_0, z_0) are space coordinates of the magnetic source, and (x, y, z) is the observation point above the magnetic source. T is the total field, B is the regional field and N is the degree of homogeneity, also known as the structural index (Thompson, 1982). For example, for a point dipole $N = 3$, for a line of dipoles $N = 2$, and for a thin dyke or pipe $N = 1$. By introducing an offset, A , (Reid et al., 1990) the above equation reduces to

$$(x - x_0) \frac{\partial T}{\partial x} + (y - y_0) \frac{\partial T}{\partial y} + (z - z_0) \frac{\partial T}{\partial z} = A \quad 3.31$$

The procedures to perform Euler deconvolution through Equations 3.30 and 3.31 on profile and gridded data are given below from Reid et al. (1990).

1. The gradients are calculated from measured data or measured directly. Hence the following are known:

$$\frac{\partial T}{\partial x}, \frac{\partial T}{\partial y}, \frac{\partial T}{\partial z}$$

2. A square window of size not less than 3×3 grid points is passed over the gradient data sets. A trial and error approach is adopted to arrive at a window size which

- gives reasonable solutions. Reid et al. (1990) found that a 10 x 10 window gives reasonable answers. However, quality (better depth estimate, with good clustering) can be increased by using smaller window sizes.
3. Once a structural index is selected (preferably non-zero), then all data points are passed through the window and using Euler's Equation 3.31 to invert for source coordinates (x,y,z), the uncertainty in the coordinates and a background value are calculated. The preferred algorithm is the Moore-Penrose inversion (Lawson and Hanson, 1974). The depth solutions are kept if the uncertainty in depth is less than 15 % of the calculated depth (Reid et al., 1990).
 4. The window is moved to the next position and Step 2 is repeated. This procedure is repeated for all possible window positions.
 5. The solutions are plotted as maps such that each solution is plotted at its plan (x,y) position using a colour proportional to depth z.

3.3.3 The significance of the Euler structural indices

The significance of the Euler structural indices for attaining correct depths solutions over magnetic bodies is well known and has been widely discussed by many workers before. As an example different geological models were prescribed structural indices ranging from 0 to 3 with reasonable success (Thompson, 1982). The significance of specific indices for particular geological models was rigorously tested by Reid et al. (1990). They observed that when they use a lower index their depth solutions were underestimated and when they use a higher index their depth solutions were overestimated. They also found that a correct index (theoretical value) does not always yield the desired solutions particularly low-index magnetic sources.

The reliance on a single structural index becomes less useful if the data contain anomalies from different sources. To overcome this problem, and hence determine the correct index for a particular feature, Reid et al (1990) proposed that one should first solve for various indices and plot the solutions for each index. The index that gives the best clustering for a

particular feature is the correct index. These principles were used to test the Euler method.

3.3.4 Euler deconvolution and wavenumber method applied to synthetic gridded data

To demonstrate the effectiveness of the methods discussed above, they were applied to synthetic data. The model consists of two bodies. The first body is a vertical dyke trending in the E-W direction. The magnetization of the dyke is 6 A/m while the depth to the top of the dyke is 10 m and the depth to the bottom is 300 m. The second body is a vertical rectangular block that with depth to top of body of 20 m and the magnetization of this body is 4 A/m. The parameters of the ambient field are: inclination = 63.8 ° and declination = 18.6 °.

Fig. 3.5 shows the magnetic response due to the synthetic model as well as the horizontal and vertical derivatives. The derivatives were calculated in the frequency domain using the fast Fourier Transform (FFT). The gridding distance along the easting and northing directions is 5 m.

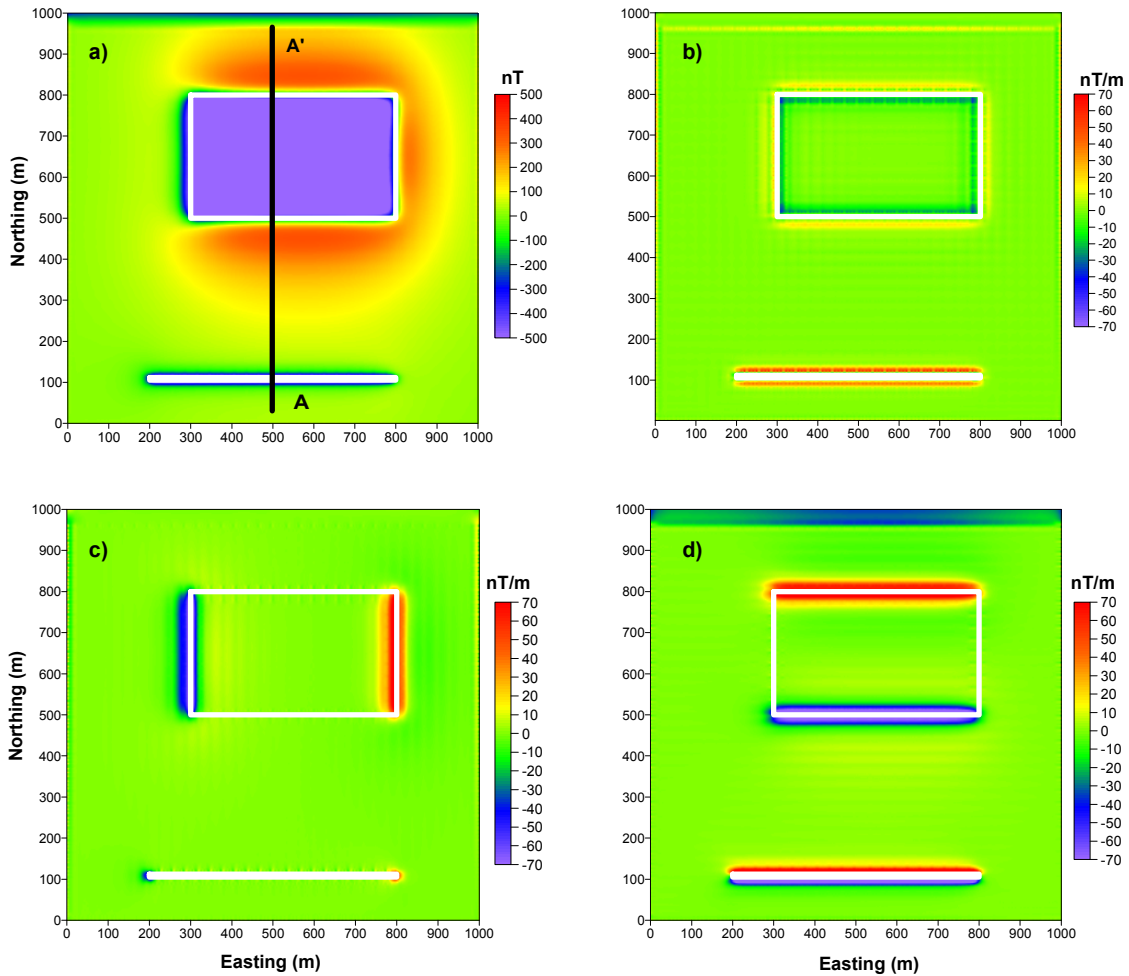


Figure 3.5. (a) The total magnetic anomaly due to the synthetic models. (b) Vertical derivative of the synthetic model. (c) x-horizontal derivative. (d) y-horizontal derivative. The outlines of the respective bodies are shown in white. Profile A-A' is used for one-dimensional depth estimates in Section 3.2.4.

Fig. 3.6 shows depth solutions using Euler deconvolution for structural indexes 0.25, 0.5, 1 and 2. The horizontal positions and the depth solutions are depicted by the dots (.) in Fig. 3.6. From the different diagrams in Fig. 3.6 we can see the effect of changing the structural index. When the structural index is 0.25 (Fig. 3.6a) the solutions plot on top of the bodies and it appears to delineate the two bodies exactly. Increasing the structural index to 0.5 (Fig. 3.6b) also has the same effect as for $SI = 0.25$ but the southern edge of rectangular body is not defined at all. For index 1 (Fig. 3.6c) and 2 (Fig. 3.6d) two observation can be made. Firstly there are too many solutions, some of which plot exactly on the edges of the bodies while the majority of the solutions plots away from the body making delineation of the body difficult. Secondly the depths associated with the rectangular body (from 30 m to 40 m) and the dyke (from 20 m to 30 m) is overestimated with respect to the original depths of 20 m (for the rectangular body) and 10 m for the dyke. Due to the non-uniqueness of the method there are a lot of redundant solutions mostly seen at the top of Figs. 3.6b-d. From this exercise it appears a that structural index of 0.25 (Fig. 3.6a) gives reliable depth estimates (from 18 to 23) for the rectangular body while the structural index of 0.5 (Fig. 3.6b) gives reliable depth estimate (from 7 m to 13 m) for the dyke.

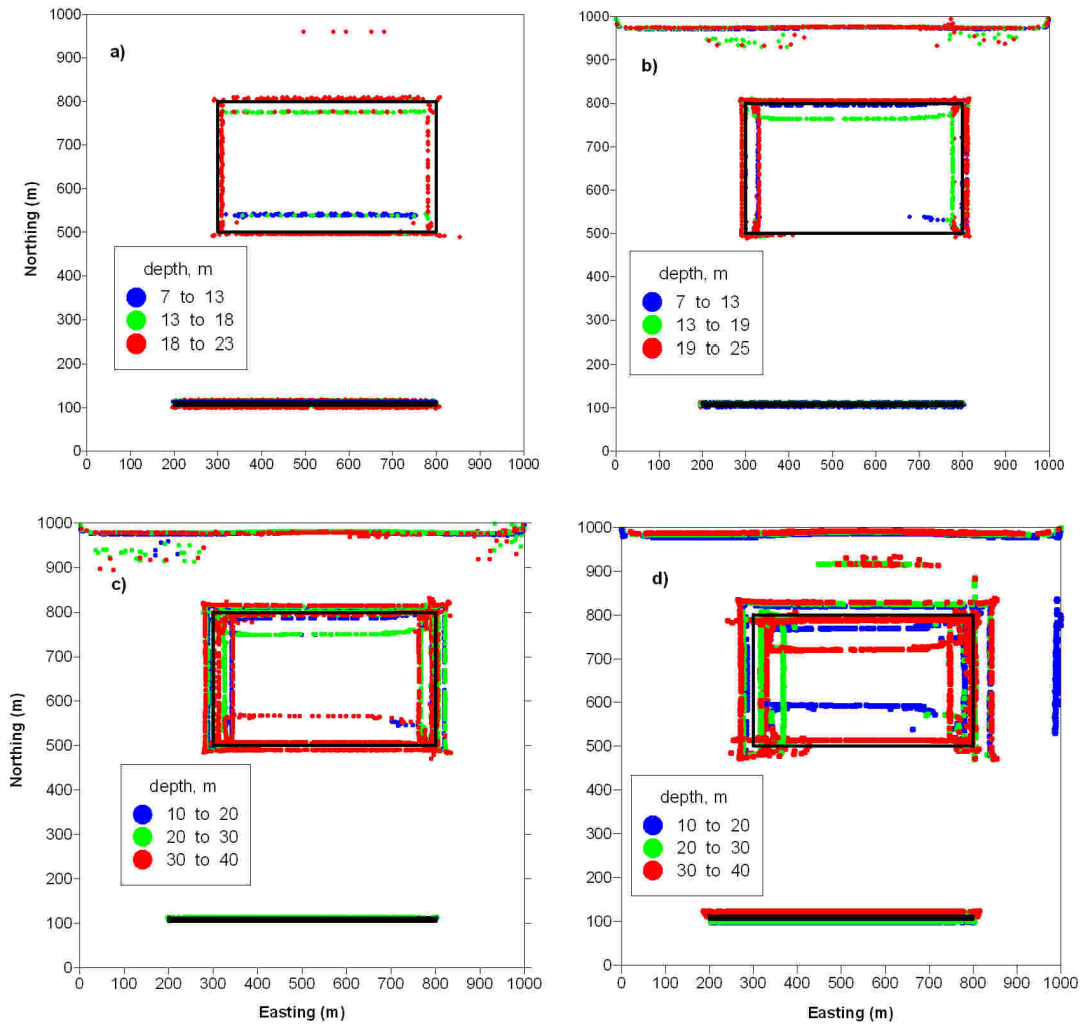


Figure 3.6. Depth estimate using a 55 m window size and tolerance of 0.75 for different structural indexes (SI). Depth estimates with (a) SI=0.25 (b) SI=0.5 (c) SI=1 and SI=2 (d). The outlines of the respective bodies are shown in black. The horizontal positions and depth solutions are depicted as dots in different colours. The horizontal positions are used to delineate the edges of the body while the colours of the dots indicate the range in depth estimates.

The next exercise involves changing the size of the window and to study the effect this has on the horizontal positions and depth estimates of the solutions. To get reliable solutions, care must be taken in choosing the size of the window. The size of the anomaly in question must be used as a guide. A small wavelength anomaly requires a small window size and long wavelength anomalies require larger window size. As a rule of

thumb, the window size should be at least half the wavelength of the anomaly in question (Reid et al., 1990; Bournas et al., 2003). These principles were used to test the Euler method.

The structural index used here is 0.25 m as the author believes this gave better results in the preceding analysis. Fig. 3.7 shows depth solutions using different window sizes. In Fig. 3.7a where the window size is 25 m the solutions plot on the edges of the bodies as defined by the black outline. For the rectangular body the depth estimate is in the range of 18 to 23 m (the red dots), but the same cannot be said for the dyke as the prevalent dots are green and red which correspond to depth ranges of 13 m to 18 m and 18 m to 23 m respectively. Increasing the window size to 30 m (Fig. 3.7b) the solutions still plot on the edges of the bodies but the depth estimates are now alternating from 13 m to 18 m and 18 m to 23 m for the rectangular body and from 7 m to 13 m and 13 m to 18 m for the dyke. In Fig. 3.7c where the window size is 50 m the southern edge of the rectangular body is not defined but the depth estimate are largely in the acceptable range (18 m to 23 m). The dyke is fairly well constrained and the depth estimate (7 m to 13 m) is also in the acceptable range. The worst result appears in Fig. 3.7d (size of window 70 m). The solutions do not appear to plot on top of the edges of the body with respect to the rectangular body. There is a spray of solutions far from the rectangular body. This could be a problem if one has to apply this to real data. On the other hand the solutions do constraint the dyke very well and also give good depth estimates.

The above analyses identify two things: edges of bodies indicated by solution points plotting on the edges of the bodies and the depth to the top of the bodies. By adjusting the structural index and the window sizes this can be accomplished to a reasonable degree.

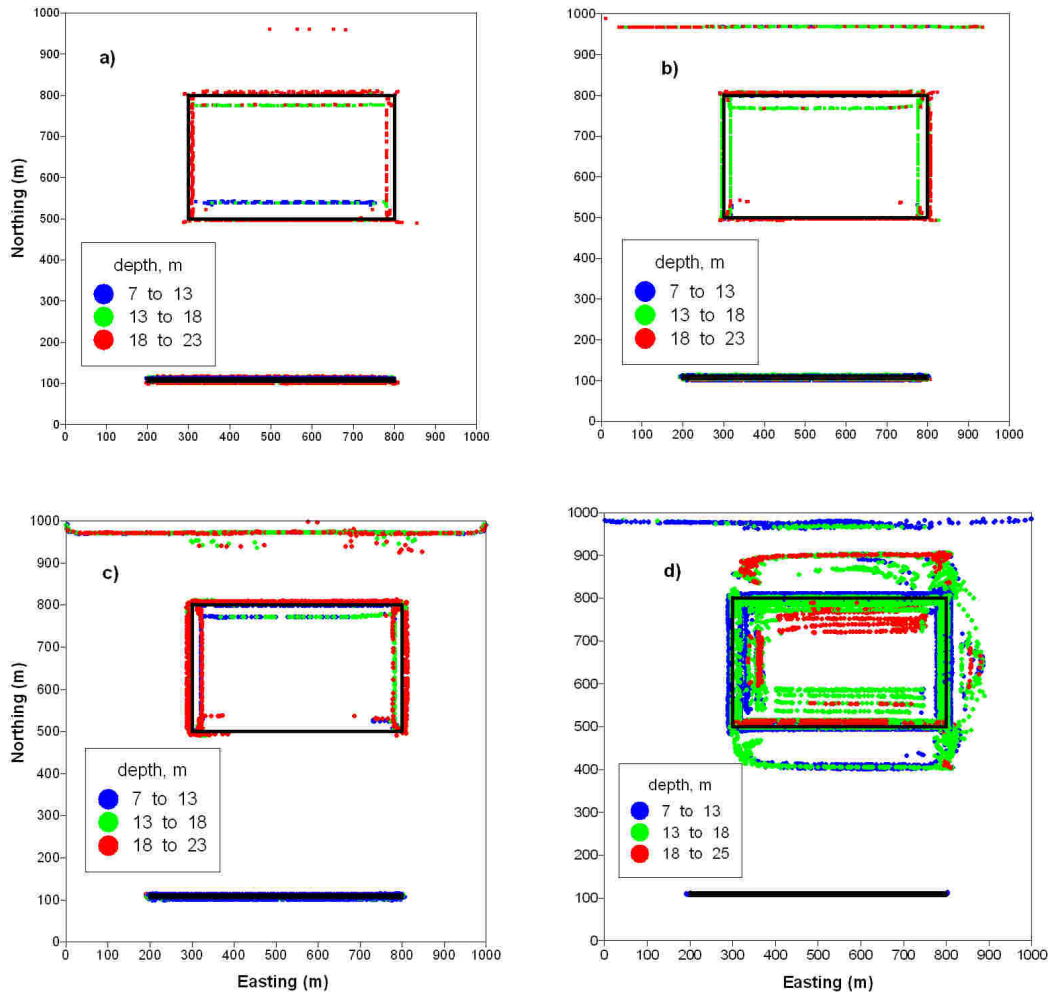


Figure 3.7. Depth estimate using a structural index $SI = 0.25$ and tolerance of 0.75 for different window sizes. Depth estimates with (a) window size 25 m (b) window size 35 m (c) window size 55 m and (d) with window size 75 m. The outlines of the respective bodies are shown in black.

The depth estimates were also determined using the local wavenumber method. This follows below. Equation 3.23 is utilized to calculate the local wavenumber. The crests of the analytical signal magnitude and local wavenumber are positioned over the centres of both bodies. To calculate the depth from the local wavenumber, the procedure described in the previous section is used. The method utilizes a 3×3 window, and calculates the maximum in four directions (horizontal, vertical and the two main diagonals). A maximum is calculated if the central value is more than the outlying values. This is tested

for all directions, and each time the criterion is satisfied a counter (N) is increased. Therefore, $N = 0$ if no maximum is found, and $N = 4$ if a maximum is found in all directions (Blakely and Simpson, 1986).

The depth solutions using the local wavenumber method are shown in Fig. 3.8. The solutions are plotted for all possible values of N. Fig. 3.8a where N is 1 shows an abundance of solutions away from the edges of the bodies. Those solutions that plot on top of the bodies indicate depth in the range of 7 m to 14 m for the rectangular body and 1 m to 7 m for the dyke. However, it is extremely difficult for one to be certain on the depth solutions as all the dots are practically superimposed on one another. The body delineation in Figs. 3.8b to 3.8d is not encouraging, but can still be used.

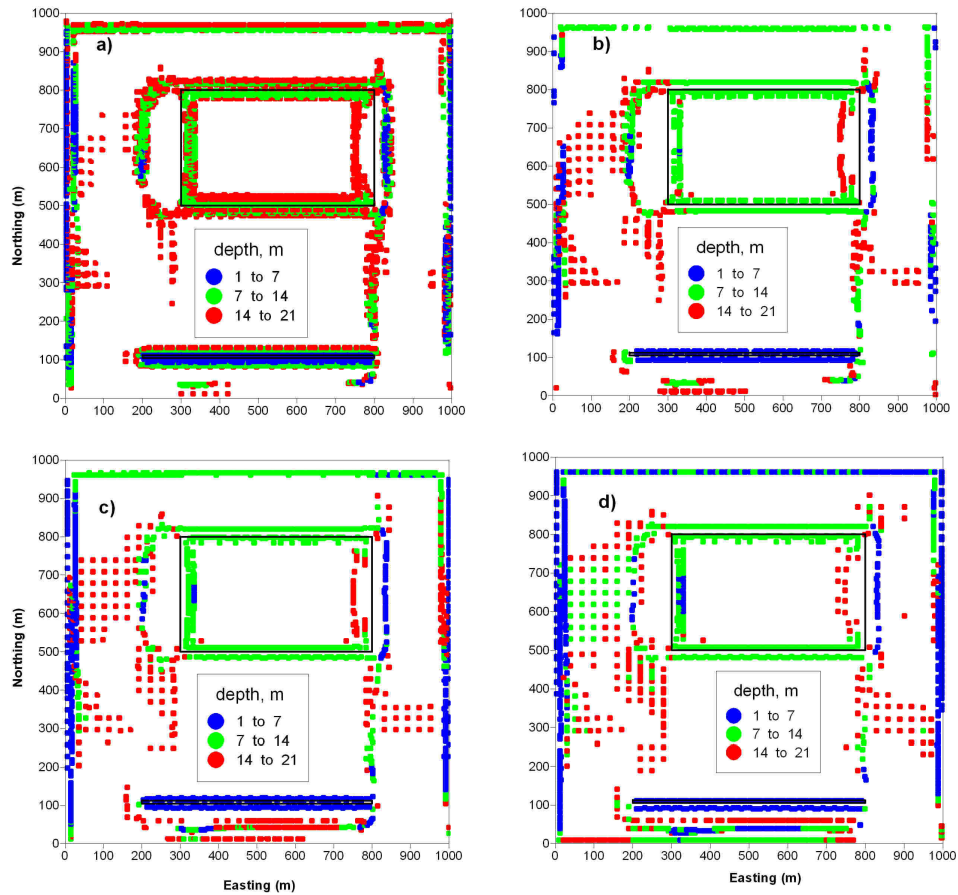


Figure 3.8. Depth estimates using the local wavenumber method. (a) $N = 1$, (b) $N = 2$, (c) $N = 3$ and (d) $N = 4$. Note that the method produces a lot of redundant solutions which are not related to any anomaly at all, such as the dots seen all over the place away from the true positions of the source bodies.

The depth estimate from the Euler deconvolution (Figs. 3.6 and 3.7) are more reasonable (closer to the depth of the synthetic models) than the depths calculated from the local wave number method (Fig. 3.8). This means that the error in depths from the local wavenumber is not acceptable. However both methods can be used to delineate the edges of causative bodies. Care must be taken in using solutions derived from the local wavenumber method.

3.3.5 Euler deconvolution and wavenumber method applied to synthetic profile data

The depth estimate from a profile extracted from the gridded data (Fig. 3.5a) is calculated in this section using both the local wavenumber method and Euler deconvolution. Fig. 3.9 shows the depth estimate using the local wavenumber method (Equation 3.27). The depth solutions are plotted as dots on the edges of the model bodies. The depths for both bodies are slightly overestimated (Fig. 3.9d and Table 3.3).

Figs. 3.10 and 3.11 show the depth solutions using the Euler deconvolution method for window lengths of 30 m and 50 m respectively. The estimates of the depth of the bodies change as the size of the window is varied from 30 m to 50 m. In Fig. 3.10 where the window length is 30 m the solutions are better constrained compared with the larger window length (Fig. 3.11) where the solutions are not well clustered. This is only evident after certain solutions are rejected. The depth estimates from the Euler deconvolution method yield better results compared with the solutions obtained from the local wavenumber method (Table 3.3).

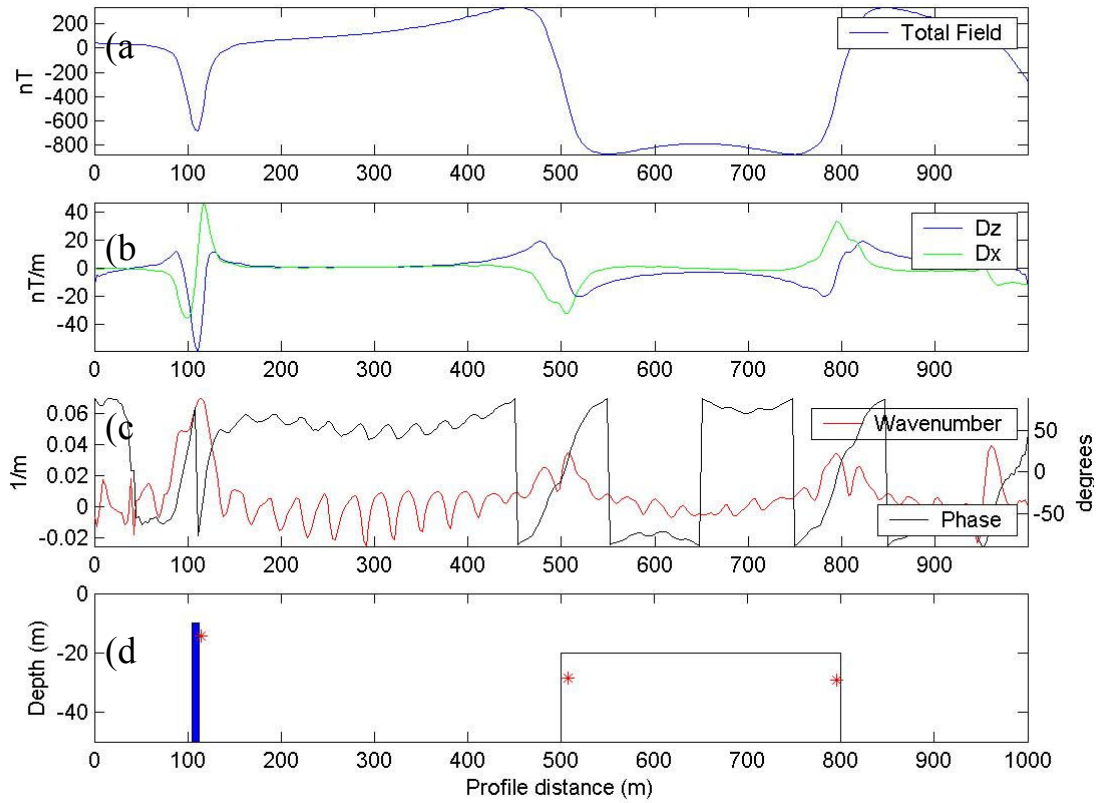


Figure 3.9. Local wavenumber depth estimates for the synthetic profile extracted from Fig. 3.5. (a) Total field anomaly profile extracted from Fig. 3.5. (b) Profiles of the vertical and horizontal derivatives of the anomaly. (c) Profiles of the wavenumber and local phase response. (d) Depth solutions superimposed on the source bodies. The local depth solutions are shown as red asterisks (*). For the dyke (blue) the local depth was calculated to be 14.30 m, and for the rectangular block (white) the average local depth was calculated as 28.90 m.

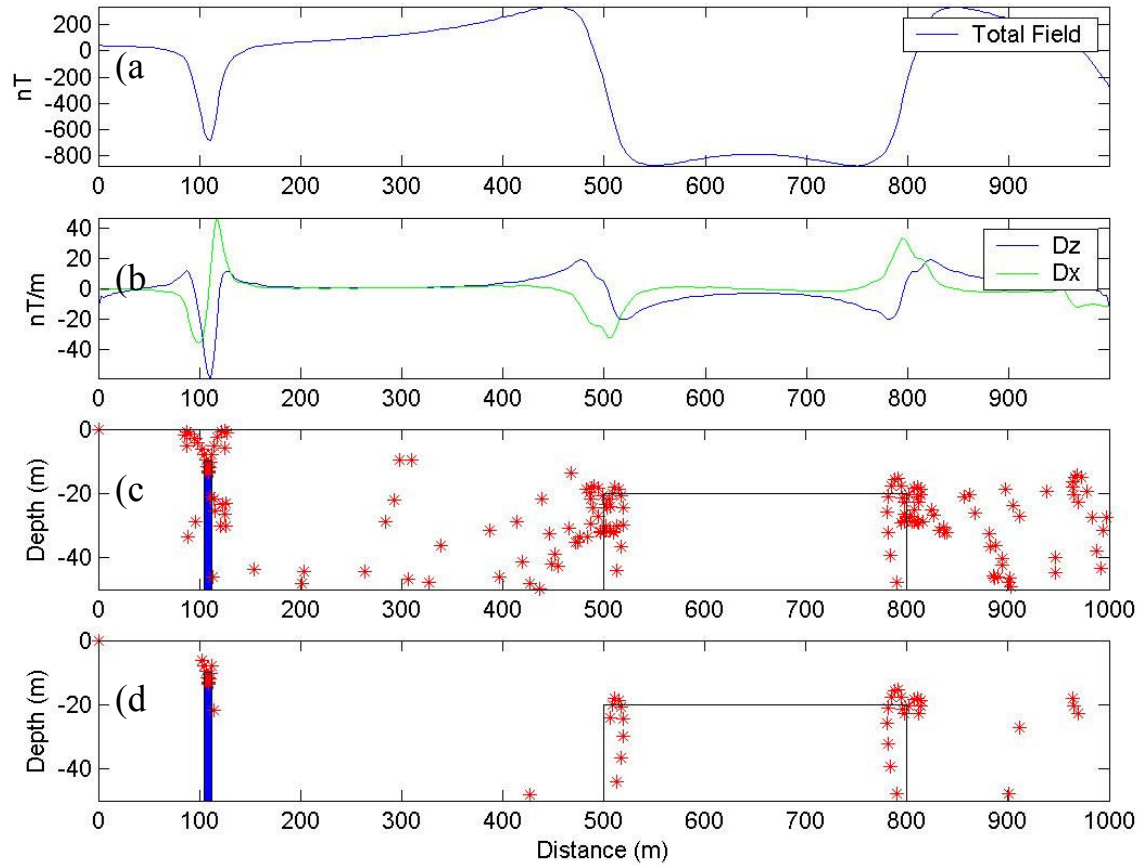


Figure 3.10. Standard Euler deconvolution depth solutions for the two bodies using a 7×7 window size. (a) Total field anomaly profile extracted from Fig. 3.5. (b) Vertical and horizontal derivatives of the anomaly. (c) Depth solutions superimposed on the source bodies. (d) Depth after rejecting solutions exceeding a tolerance level of 0.15. The depths solutions are shown as red asterisks (*). The structural index was $SI = 1$.

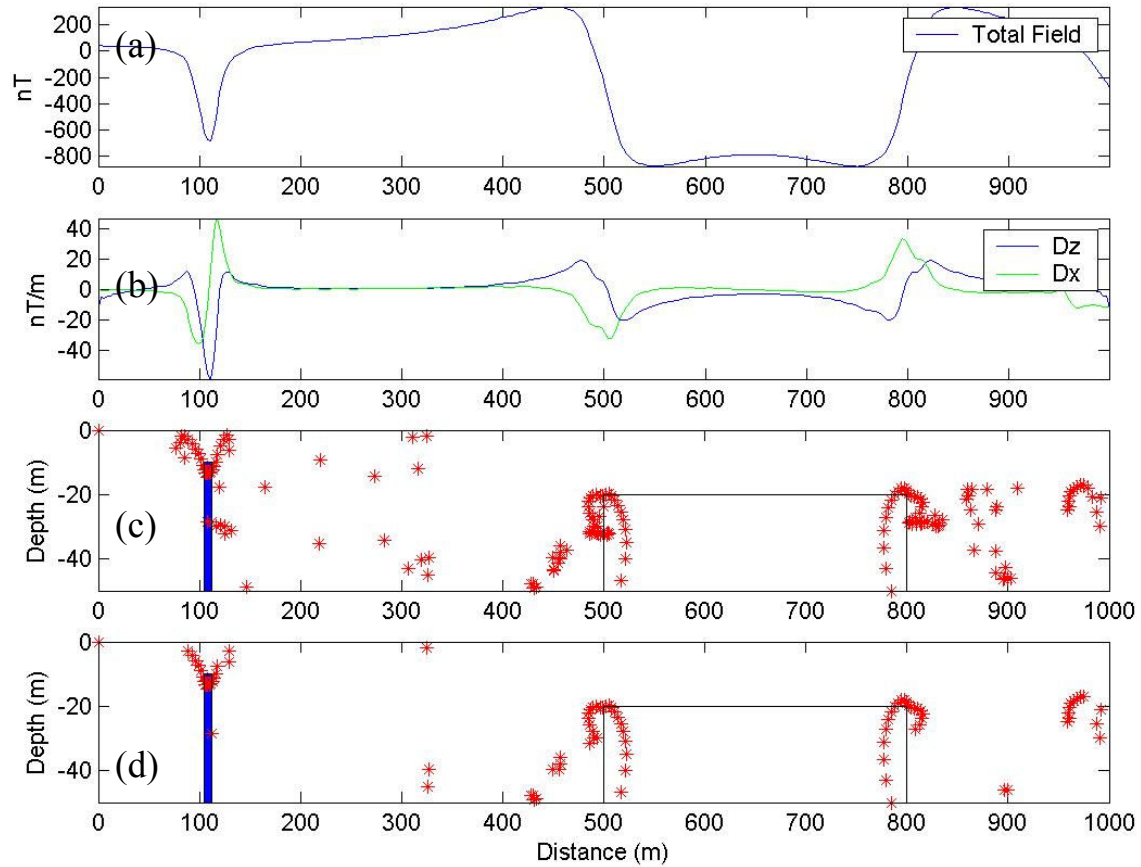


Figure 3.11. Standard Euler deconvolution depth solutions for the two bodies using an 11x11 window size. (a) Total field anomaly profile extracted from Fig. 3.5. (b) Vertical and horizontal derivatives of the anomaly. (c) Depth solutions superimposed on the source bodies. (d) Depth after rejecting solutions exceeding a tolerance level of 0.15. The depths solutions are shown as red asterisks (*). The structural index was $SI = 1$.

Table 3.3. Summary of depth estimates using the local wavenumber (LW) and Euler deconvolution (ED) methods for the synthetic profile data. The error is the difference between the true value given in the text and the calculated depths from the respective methods.

Source	LW (m)	Error LW (m)	ED (m)	Error ED (m)
Dyke	14.30	4.30	13	3
Contact/rectangular block	28.90	9	19	1

3.4 Summary

Upward continuation of synthetic data emphasizes long wavelength anomalies while de-emphasising short wavelength anomalies. The upward continuation method works quite well and this will be used in comparing ground magnetic data from this study with aeromagnetic data from the same area. Hidden features are revealed by the use of the AGC algorithm. This appears to be a suitable method in bringing out subtle features while retaining long-wavelength anomalies.

Two depth estimation methods were compared and applied to synthetic data. The methods are the local wavenumber and Euler deconvolution. For gridded data, the Euler deconvolution method delineates the bodies and gives reliable depth estimates while the local wavenumber method does not delineate the bodies that well and the depth estimates are underestimated. For Euler deconvolution, a good estimate of depth depends on the choice of the structural index, tolerance and size of the window. Depth estimates using the local wavenumber are overestimated for both gridded and profile data. However the margins of errors are acceptable.